ECS Journal of Solid State Science and Technology, 2025 **14** 094002
2162-8777/2025/14(9)/094002/8/$40.00

Structural Properties and Raman Spectra of Micron-Thick β-Ga_2O_3 Films Deposited on SiC/Porous Si/Si Substrates

V. V. Kidalov,[1,2] M. P. Derhachov,[3,z] A. S. Revenko,[4] O. I. Gudymenko,[5] R. A. Redko,[5] O. O. Sushko,[3] M. M. Koptiev,[3] M. A. Assmann,[1] and R. P. Johnson[4]

[1]*Experimentelle Physik 2, Technische Universität Dortmund, Dortmund 44221, Germany*
[2]*Dmytro Motornyi Tavria State Agrotechnological University, Zaporizhzhia 69063, Ukraine*
[3]*Oles Honchar Dnipro National University, Dnipro 49045, Ukraine*
[4]*School of Chemistry, University College Dublin, Belfield, Dublin 4, Ireland*
[5]*V. Lashkaryov Institute of Semiconductor Physics NAS of Ukraine, Kyiv 03028, Ukraine*

The possibility of expanding the element base of optoelectronics and power electronics by using β-Ga_2O_3 motivates the search for efficient methods for growing its high-quality films. Here, β-Ga_2O_3 films with thicknesses of 1.15 and 2.25 μm were deposited on SiC/porous Si/Si substrates using high-frequency magnetron sputtering and characterized by scanning electron microscopy, X-ray diffraction (XRD), and micro-Raman spectroscopy techniques. The films were composed of β-Ga_2O_3 crystallites with an average size of 62 and 109 nm, preferentially oriented along [100] direction. The relative increase of their lattice parameters with respect to single crystal ones was no more than 1.5×10^{-3} for the *c* parameter. The small strain values of about 1×10^{-3} calculated from the XRD patterns were verified by the absence of any significant changes in phonon modes' parameters in the β-Ga_2O_3 film Raman spectra.
 [DOI: 10.1149/2162-8777/adfb52]

Manuscript submitted March 29, 2025; revised manuscript received June 9, 2025. Published September 8, 2025.

Modern trends in scaling of Si-based micro- and optoelectronic devices involve the search for new materials, possessing, among other properties, a high value of dielectric constant (k), enough to replace SiO_2 in the metal oxide semiconductor (MOS) structures.[1,2] Various metal oxide materials such as Yb_2O_3,[3] γ-Al_2O_3,[4] NiOx,[5] TiO_2,[6] HfO_2,[7,8] ZrO_2[8,9] have already been successfully synthesized on Si substrates. Gallium oxide (Ga_2O_3) can be confidently added to that lineup. Belonging to the *C*2/*m* space group,[10] this wide-bandgap material (E_g is varied from 4.26 eV to 5.24 eV, depending on whether it is bulk or film[11]) exhibits strong resistance to electrical impact (the breakdown field is 8 MV cm^{-1} and k is 10) as well as excellent chemical and thermal stability.[12] The β-phase of gallium oxide can be easily doped, which makes it possible to obtain well-conducting layers.[13,14] Its Young's modulus—ranging from approximately 240 GPa to 270 GPa—provides sufficient rigidity for use in high-frequency nanoresonators. Its low mass and reasonable fracture strength make it particularly attractive for sensitive components in micro- and nanoelectromechanical devices. Nevertheless, its relatively low fracture toughness and thermal conductivity require careful consideration when designing high-power circuits.[12] Due to all these factors, the fabrication of the high quality β-Ga_2O_3 layers and heterostructures based on them is receiving more and more attention.[15–19] To date, it is known about the creation of energy-efficient LEDs, Schottky diodes, solar-blind ultraviolet photodetectors, field-effect transistors, gas sensors, and the possibility of producing high-voltage transistors on the basis of β-Ga_2O_3 epitaxial layers.[20–26]

Since silicon remains one of the base materials of microelectronics, investigations aimed at synthesizing epitaxial β-Ga_2O_3 films on Si substrates are of particular practical interest.[27] However, it is very difficult to produce such films directly on the silicon surface. In an oxygen atmosphere at high temperature, an amorphous silica layer is formed on the silicon surface and the epitaxial film will not grow on such a substrate. To prevent oxidation, it is possible to use Si substrates with a pre-coated buffered epitaxial layer of silicon carbide. Silicon carbide (SiC) is a wide-bandgap semiconductor material with a large number of polytypes given by the various stacking sequences of Si and C atoms in its structure.[28] The most popular, hexagonal 4H-SiC and 6H-SiC polytypes are stable at very high temperatures and have significant advantages over Si in the values of important parameters at room temperature: a wider band gap (approximately 3.26 eV as opposed to 1.1 eV), a higher breakdown field (3 MV cm^{-1} compared to 0.3 MV cm^{-1}) and a greater thermal conductivity (5 W $(cm\ K)^{-1}$ up against 1.5 W $(cm\ K)^{-1}$).[29] Besides, SiC has exceptional mechanical strength, hardness and chemical stability, which contributes to its durability and reliability in harsh environments.[29,30] Being deposited on Si substrate, SiC films can be successfully used in designing high-performance ultraviolet detectors.[31] Current research continues to confirm the enormous potential of SiC in areas such as power electronics, complementary metal oxide semiconductor (CMOS) technology and various energy applications, laying the foundation for its continued growth in commercial use.[29,32]

Although high-frequency magnetron sputtering (HFMS) has been effectively utilized to deposit β-Ga_2O_3 films with controlled thickness and desirable crystalline properties, a comprehensive evaluation of its performance relative to alternative techniques is essential for assessing its practical value. Commonly employed methods for β-Ga_2O_3 film growth include pulsed laser deposition (PLD), molecular beam epitaxy (MBE), metal-organic chemical vapor deposition (MOCVD), and mist-CVD.[16,17,33,34] Each technique offers distinct advantages in terms of film quality, deposition rate, scalability, and equipment complexity. For instance, MBE and MOCVD can produce high-purity, epitaxial films with excellent control over stoichiometry and doping but require complex, high-vacuum environments and are limited in throughput. Conversely, PLD allows for high-fidelity stoichiometric transfer but suffers from poor uniformity over large areas. HFMS, in contrast, offers a balance between quality and scalability, operating at lower substrate temperatures and enabling deposition over larger substrates with relatively simple equipment. Additionally, magnetron sputtering enables better control of film stress and adhesion, which is particularly relevant when targeting mechanical robustness in MEMS or power device applications. When compared to these alternatives, HFMS emerges as a versatile and cost-effective approach, especially suitable for industrial-scale deposition of β-Ga_2O_3 films with moderate to high crystalline quality.[19,35]

In our earlier paper[36] we used successfully this technique to deposit β-Ga_2O_3 films on the porous Si/Si substrates. In this work, we discuss fabrication of the micron-thick β-Ga_2O_3 films on SiC/porous Si/Si substrates as well as define their structural parameters and quality by scanning electron microscopy (SEM), X-ray diffraction (XRD) and micro-Raman spectroscopy techniques.

[z]E-mail: derhachov.mp@gmail.com

Experimental

The fabrication process of the Ga_2O_3/SiC/porous Si/Si structure consisted of three sequential stages: (1) formation of a porous layer on the Si wafer surface, (2) deposition of a SiC film on the porous surface, (3) deposition of a Ga_2O_3 film on the formed substrate.

Porous Si/Si substrates were obtained from Smart Membranes GmbH (Germany). The porous layer was formed by electrochemical etching of the original Si wafers with surface orientation along the (100) or (111) plane. As shown in papers,[37,38] there is a strong anisotropy of the electrochemical etching rate in crystalline silicon because the [111] crystallographic direction is not the preferred direction for pore growth. While pores in (100)-oriented Si wafer grow perpendicular to the surface, along the [100] directions, those in (111)-oriented wafer propagate along the [100] directions inclined by approximately 55° relative to normal to the surface. In order to compensate for the different etching rates and to achieve layers with comparable thicknesses and pore diameters, different technological parameters were employed for (100)- and (111)-oriented Si wafers. Pore diameters were measured from SEM images, where pores appeared as darker regions, using ImageJ software (National Institutes of Health, USA). The resulting data were used to construct histograms illustrating the distribution of pore sizes and their corresponding frequencies. The depth of the porous layer was determined using cross-sectional SEM imaging. According to that, the mean pore diameter was approximately 17 nm, and the depth of the porous layer was about 240 nm.

SiC films were deposited on porous Si/Si substrates by atomic substitution method.[39,40] The process involved the reaction between gas compounds such as CO and SiH_4 at high temperatures, which leads to the formation of a SiC layer on the porous silicon surface.[41] For this purpose, air was first removed from the vacuum chamber to 10^{-2}–10^{-3} Pa using a 2NVR-5DM rotary pump, after which the sample was heated with a graphite heater to a temperature of 950 °C to 1290 °C. The next step was to feed a mixture of CO and SiH_4 into the chamber using a HORIBA gas regulator with a total pressure of 130 Pa at flow rates of 15 $cm^3\,min^{-1}$ for CO and 3 $cm^3\,min^{-1}$ for SiH_4. The deposition duration was from 20 min to 60 min. The mechanism of SiC films production on porous Si substrates was described in more detail in our previous paper.[42]

Gallium oxide films were deposited by high-frequency magnetron sputtering of 99.995% pure Ga_2O_3 in a high-purity argon atmosphere at a constant chamber pressure of about 3×10^{-3} Pa (or 2 mTorr). The time required to grow films with thickness between 1 μm and 2 μm was estimated from our earlier results,[36] assuming a linear dependence for the film thickness, and ranged from 250 min to 350 min. Deposition was performed on SiC/porous Si/Si substrates heated up to 200 °C. After deposition, all samples were annealed for two hours in the air atmosphere at 850 °C.

Visual inspection of all obtained structures was performed using a TESCAN MIRA 3 lMU scanning electron microscope. The elemental composition of the SiC/porous Si/Si substrates was determined by an Oxford Instruments INCA Energy 350 X-max 80 energy dispersive microanalyzer.

XRD measurements were performed by PANalitical X Pert Pro with Cu Kα_1 radiation ($\lambda = 1.5406$ Å). The grazing-incidence XRD (GIXRD) patterns as well as the symmetric $2\theta/\omega$ scans were obtained to define structural properties of Ga_2O_3 films and SiC/porous Si/Si substrates, respectively. The symmetric $2\theta/\omega$ scans were measured using a four-crystal Ge (220) monochromator.

Micro-Raman spectroscopy was used to identify the structural phase and crystal quality of Ga_2O_3 films grown on SiC/porous Si/Si substrates. The Raman measurements were acquired in a quasi-backscattering geometry using the Horiba Jobin-Yvon T64000 triple spectrometer with integrated micro-Raman setup—Olympus BX-41 microscope equipped with a motorized XYZ stage (at minimum step of 0.1 μm) and Peltier-cooled CCD detector. The experiments were conducted at room temperature using the 532 nm line of diode-pumped solid-state laser (Spectra-Physics).

Results and Discussion

SEM images of SiC layers deposited on the porous Si/Si substrates with differently oriented Si wafers are shown in Fig. 1. Within the examined surface area, the SiC layer thickness varies slightly and is, on average, 120 nm for the film grown on the Si (100) wafer (Fig. 1b) and 51 nm for that on the Si (111) wafer (Fig. 1d), with deviations from the mean value no more than 5 nm. Such differences in the SiC layer thickness are reasonably attributed to the different surface orientation of the silicon wafer. As shown in paper,[43] thermodynamic stability and atomic bonding configurations of the surface are the main factors that underline the critical role of crystallographic orientation in controlling the morphology and thickness of SiC layers synthesized via the atomic substitution method. Si (111) surface is more densely packed and energetically more stable than Si (100) surface, which leads to a reduced substitution rate and, consequently, a thinner SiC layer. Furthermore, the higher surface energy and lower atomic density of Si (100) surface promote a more efficient atomic substitution process, resulting in thicker SiC films. Thus, under identical growth conditions, the SiC layer formed on Si (111) wafer should tend to be thinner compared to that on Si (100) wafer.[43,44]

SEM images of Ga_2O_3 films grown on the SiC/porous Si/Si substrates are represented in Fig. 2. As can be seen from there, the obtained gallium oxide films consist of crystallites in the form of oblique parallelepipeds or even plane-parallel plates inclined to the substrate surface at an angle in the range of 29°–39° for the film in Fig. 2a and 64°–70° for the other one (Fig. 2b). Different thicknesses of the films, in this case, are due to the different durations of their deposition. The thicker (2.25 μm) Ga_2O_3 film was deposited on the substrate with Si (100) wafer for 330 min (Fig. 2a), while the thinner (1.15 μm) Ga_2O_3 film was grown on the substrate with Si (111) wafer in 262 min (Fig. 2b). In both structures, the Ga_2O_3 film thickness exceeds the SiC layer thickness by almost 20 times. As with the SiC layer, variation of the film thickness within the examined surface area is not significant and does not exceed 7 nm. Hereinafter, the 2.25 μm Ga_2O_3/120 nm SiC/Si (100) structure will be referred to as "S1 structure" (Fig. 2a) and the 1.15 μm Ga_2O_3/51 nm SiC/Si (111) structure will be called "S2 structure" (Fig. 2b).

As expected, the SiC layer prevents the formation of amorphous silica on the Si wafer surface. The obtained SEM images do not indicate the presence of oxide layer. In accordance with the EDAX spectroscopy results, the silicon content in the SiC/porous Si/Si substrates is, on average, 80.7 wt% and the carbon is 17.6 wt%. Finally, a wide diffuse halo, which is typical for amorphous silica phase and centered at about 22° on the two-theta scale, is not observed in both the symmetric $2\theta/\omega$ scans (Fig. 3) and the GIXRD patterns (Fig. 4).

The symmetric $2\theta/\omega$ scans contain intensive crystalline Si and SiC peaks and also weak, sometimes barely visible, peaks of the Ga_2O_3 phase (Fig. 3). Most intensive XRD peaks at 69.10° and 28.22° are related to the (400) and (111) Si peaks, verifying the (100) and (111) wafer surface orientation in the S1 and S2 structures, respectively. Silicon carbide is manifested only in the S2 pattern as peaks at 35.66° and 75.47°, which are due to the X-ray diffraction on the sets of (111) and (222) planes of the cubic SiC phase (curve 2 in Fig. 3). The appearance of these peaks suggests pseudomorphism of the SiC layer with respect to the Si wafer. In the case of polycrystallinity, the SiC peaks should be observed in the GIXRD patterns too, but they are not present there (Fig. 4).

The GIXRD patterns of the S1 and S2 structures are in complete agreement with the reference data for β-Ga_2O_3 single crystals (PDF2 #010-87-1901) regarding the angular positions of peaks. On the contrary, the intensity of a number of peaks, especially in the range of 29°–40° on the two-theta scale, significantly differs both from the reference data and when comparing the measured patterns with each other (Fig. 4 and the inset therein). Such behavior may indicate the occurrence of texture, the presence of the fractions of crystallites with the preferred orientation. Based on that assumption, we engaged the

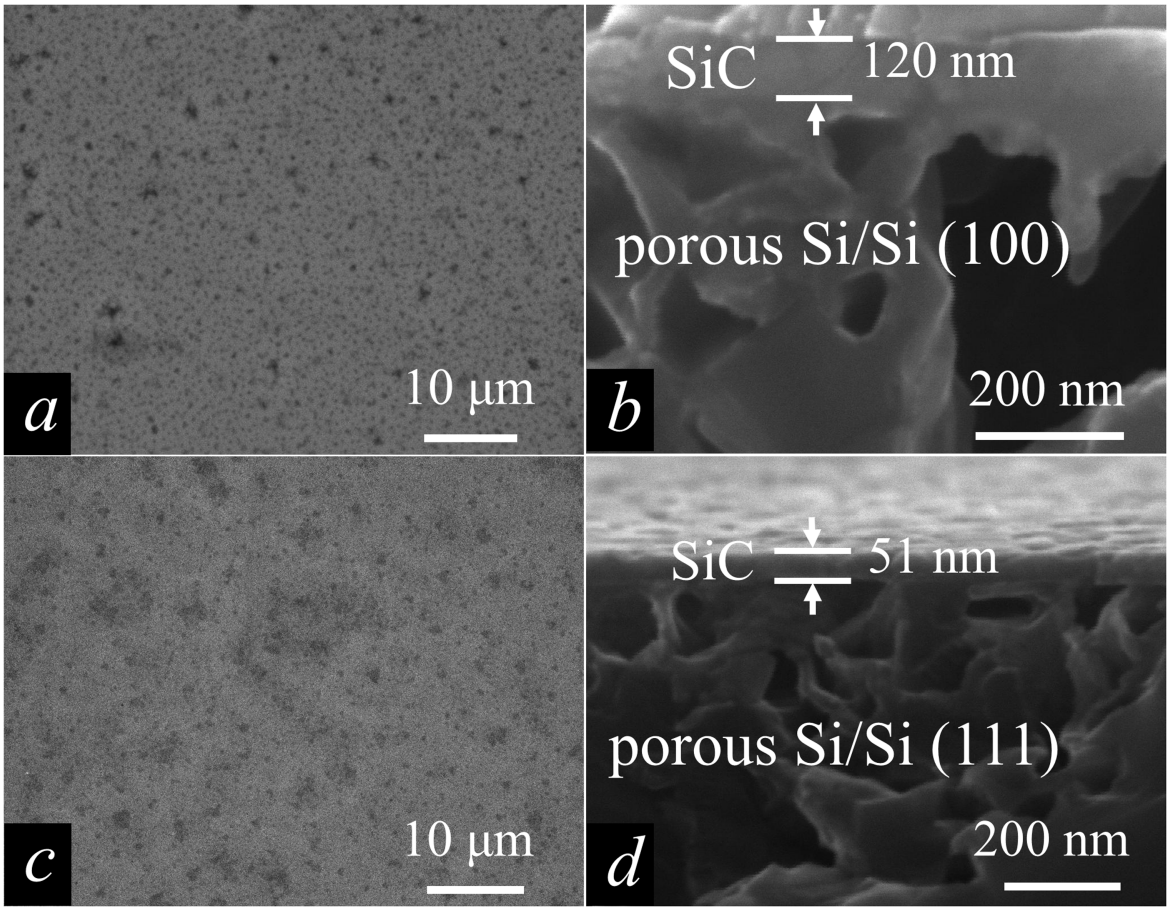

Figure 1. Plan view and cross-section SEM images of the SiC layers on the porous Si/Si substrates with differently oriented wafer surfaces: *a*, *b*–Si (100); *c*, *d*–Si (111).

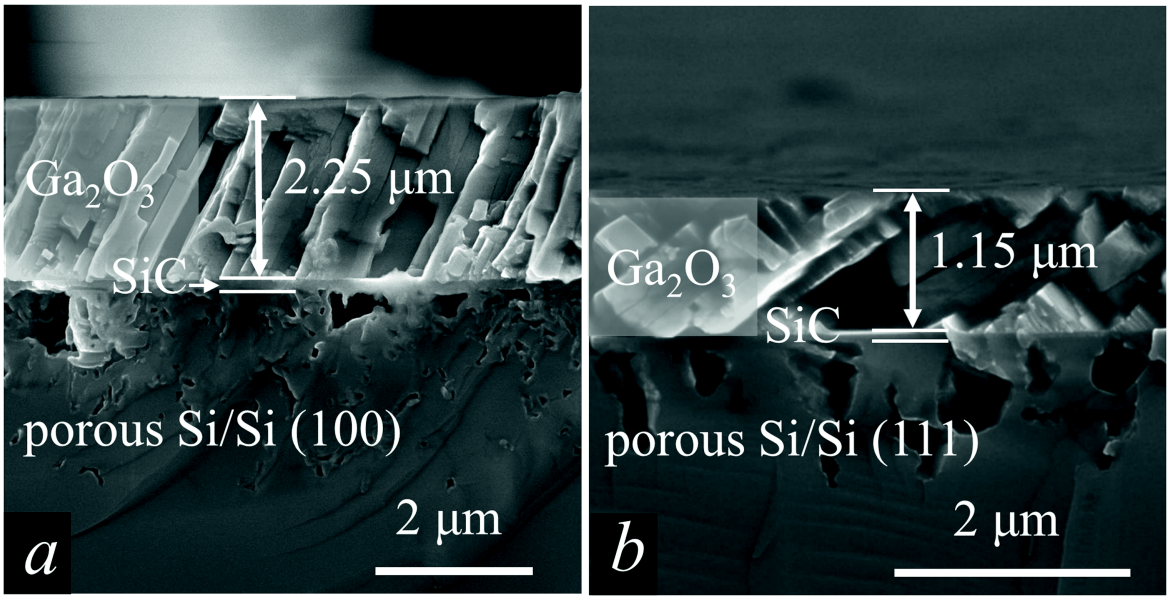

Figure 2. Cross-section SEM images of the Ga_2O_3/SiC/porous Si/Si structures with differently oriented wafer surfaces: *a*–Si (100); *b*–Si (111).

March-Dollase multi-axial model,[45] when performing the full profile Rietveld refinement using FullProf Suite package. To estimate the degree of preferred orientation, we choose the parameter η, introduced by E. Zolotoyabko[46] and defined through the March parameter r as follows

$$\eta = (1 - r)^{3/2}(1 - r^3)^{-1/2} \times 100\%. \quad [1]$$

The best agreement with the experimental data is achieved when considering two preferred orientations for the S1 structure, along

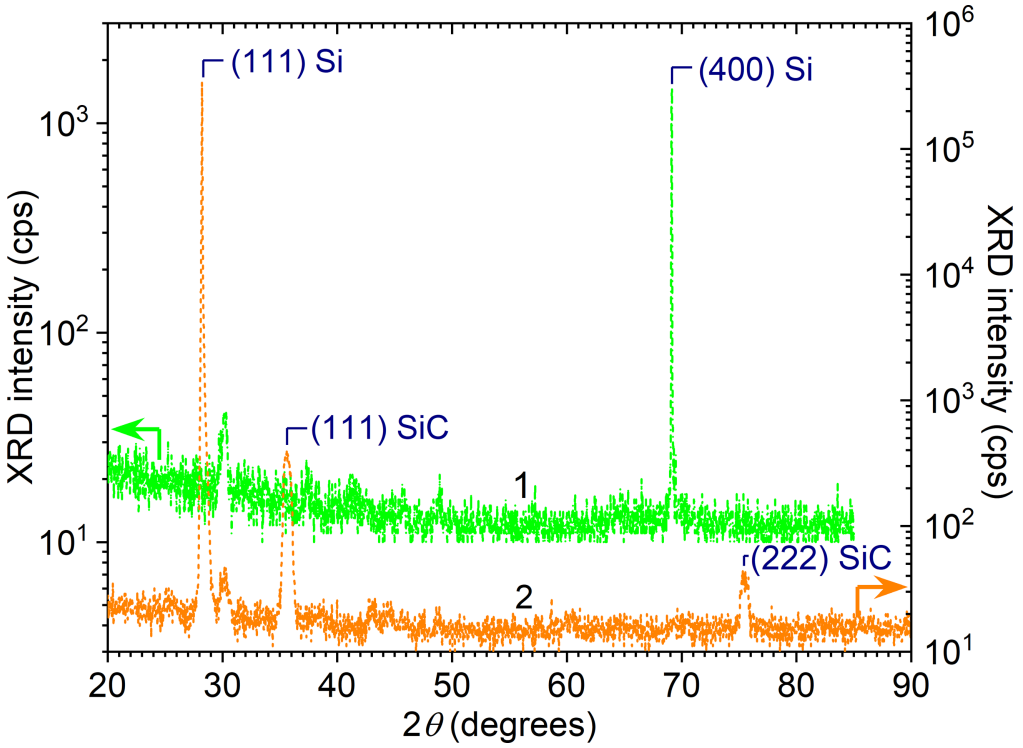

Figure 3. Symmetric $2\theta/\omega$ scans of the S1 (1) and S2 (2) structures.

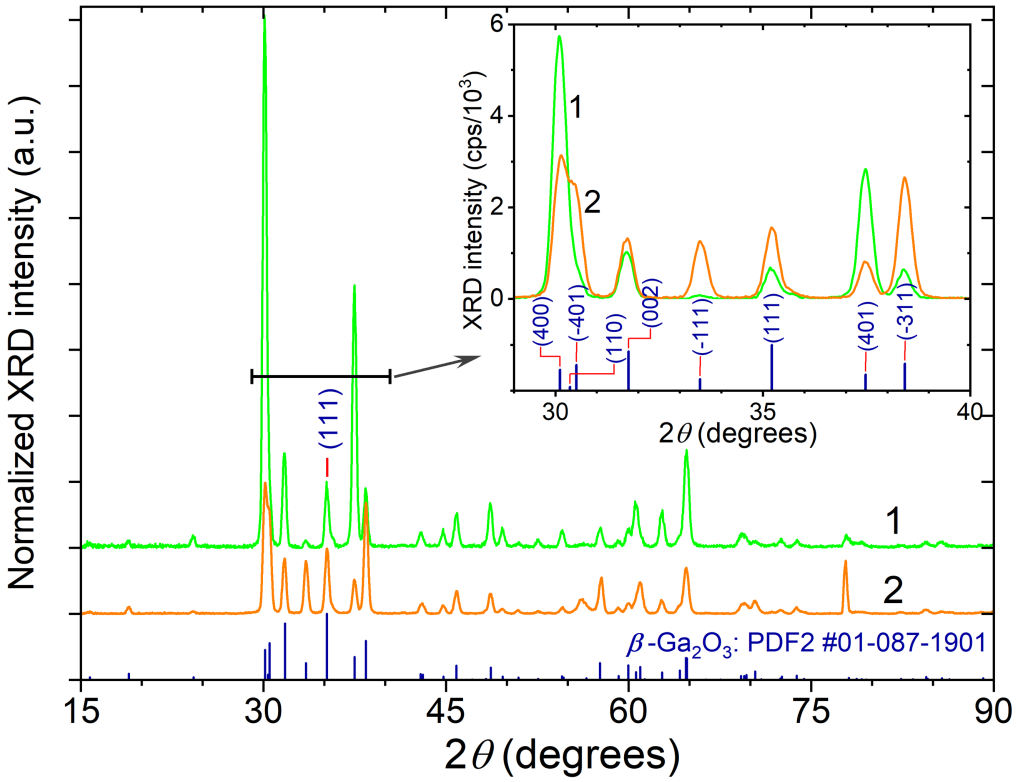

Figure 4. GIXRD patterns of the S1 (1) and S2 (2) structures together with reference data for β-Ga_2O_3 (PDF2 #010-87-1901). All the patterns are normalized by the corresponding intensity of the (111) peak, the highest one for the reference data. The inset presents the intensity redistribution in the patterns with indicating reference peaks.

[100] ($\eta = 62\%$) and [401] ($\eta = 24\%$) directions, and three preferred orientations for the S2 structure, along [100] ($\eta = 47\%$), [101] ($\eta = 23\%$) and [201] ($\eta = 21\%$) directions. Nevertheless, even the March-Dollase approach does not allow us to attain the proper intensities of some peaks positioned at about 48.6°, 57.8°, 60.5° and 64.8° in the corresponding XRD patterns (Fig. 5). Besides, two peaks within the ranges of 55.3^0–57.1^0 and 77.2^0–78.4^0 for the S2 pattern are excluded from the calculations as those that cannot be described

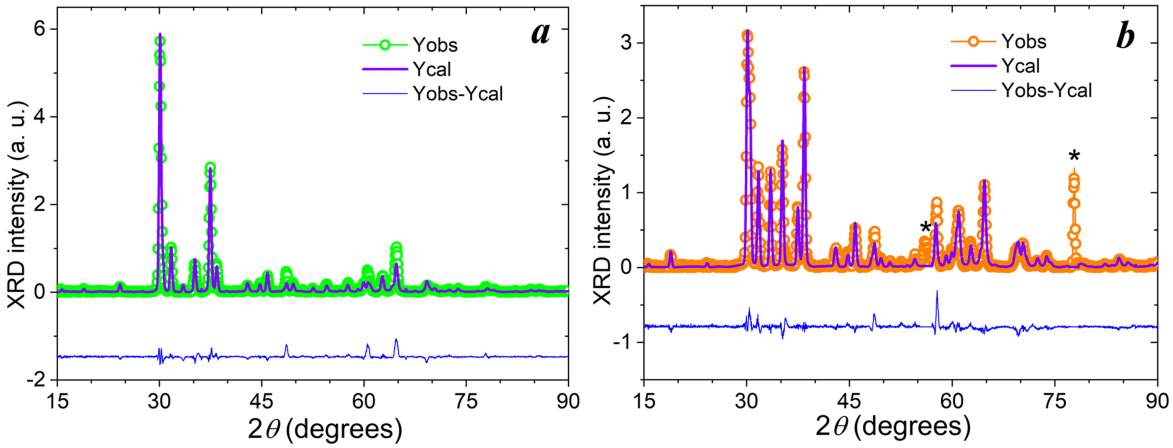

Figure 5. The Rietveld refinement results for the S1 (*a*) and S2 (*b*) structures. The measured GIXRD patterns are plotted by green and orange dotted curves, and the calculated profile by the violet one (Ycal). The bottom blue curve represents the differences between the experimental and the calculated data. The peaks, marked with asterisks, are excluded from the calculations.

Table I. β-Ga_2O_3 film lattice parameters and their relative changes.

	β-Ga_2O_3 film			Relative changes	
Lattice parameters	S1	S2	β-Ga_2O_3 single crystal[10]	S1	S2
a (Å)	12.2194(6)	12.2237(8)	12.214(3)	0.44×10^{-3}	0.79×10^{-3}
b (Å)	3.0371(4)	3.03812(2)	3.0371(9)	0.00	0.34×10^{-3}
c (Å)	5.8032(6)	5.80662(5)	5.7981(9)	0.88×10^{-3}	1.47×10^{-3}
V (Å^3)	209.103(36)	209.364(27)	208.85(9)	1.21×10^{-3}	2.46×10^{-3}

within the applied model in any way. The origin of these peaks, marked with asterisks in Fig. 5, remains to be elucidated.

The lattice parameters of the β-Ga_2O_3 films, refined with the Rietveld methodology by using the program package FullProf Suite,[47] and their relative changes with respect to single crystal patameters[10] are listed in Table I. To calculate the crystallite size D and strain ε we apply the Williamson-Hall method within the uniform deformation model by exploiting the equation[48,49]

$$B\cos\theta = \lambda/D + 4\varepsilon\sin\theta, \qquad [2]$$

where θ and B are the angular position and full width at half maximum (FWHM) of the corresponding (*hkl*) diffraction peaks. Considering Eq. 2 as a linear approximation of the set of values of θ and B on the $B\cos\theta$ vs $4sin\theta$ graph (Fig. 6), we estimate the corresponding D and ε values as well as the dislocation density δ in terms of the domain contribution, $\delta = D^{-2}$ (Table II).

Now, let us consider the Raman spectra of the obtained structures. As mentioned above, β-Ga_2O_3 single crystal belongs to the monoclinic system with the corresponding C_{2h} point symmetry group.[10] In accordance with the theoretical analysis for this group, irreducible representation for optical phonons at the Γ-point, corresponding to the center of the Brillouin zone, can be written as follows[50]

$$\Gamma_{opt} = 10A_g + 5B_g + 4A_u + 8B_u, \qquad [3]$$

where A_g and B_g modes are Raman-active, A_u and B_u ones are infrared active.

In our case, without analyzing the polarization state of the scattered radiation, we quite clearly reveal all of these 15 Raman-active modes in the spectrum of the S1 structure (green curve in Fig. 7). As for the other structure, a larger number of Raman bands is observed (orange curve in Fig. 7). The appeared bands are related to the substrate contribution and assigned to the vibrations

Table II. β-Ga_2O_3 film structural parameters.

Parameter	S1	S2
Crystallite size D (nm)	109 ± 20	62 ± 6
Strain ε	$(0.94 \pm 0.17) \times 10^{-3}$	$(0.56 \pm 0.15) \times 10^{-3}$
Dislocation density δ (m^{-2})	$\approx 8.4 \times 10^{13}$	$\approx 2.6 \times 10^{14}$

in the Si and SiC lattices.[51–53] Such different contributions from the substrates, more prominent for a thicker film in the S2 structure, can be primarily attributed to the different orientation of the Si wafer surface relative to the incident laser beam. This orientation specifies the Raman tensor components α_{ij} and, consequently, band intensities. The silicon Raman bands positioned within the 200 cm^{-1}–450 cm^{-1} and 900 cm^{-1}–1050 cm^{-1} ranges are most intensive for the component α_{xx}.[51] This component cannot be observed in the spectrum of the S1 structure with the Si (100) wafer, but it is available to be detected in the spectrum of the Si (111) wafer.

The S1 and S2 Raman spectra are plotted in Fig. 7 together with the results of their fitting performed within the framework of the model of weakly-coupled oscillators with the following equation[54]

$$J(\omega, T) = [n(\omega, T) + 1] \times \sum_{j=1}^{N} I_j \omega\omega_j^2\gamma_j/((\omega_j^2 - \omega^2)^2 + \omega^2\gamma_j^2) + y_0. \qquad [4]$$

Herein, $J(\omega, T)$ is the spectral intensity, $n(\omega, T)$ is the Bose–Einstein factor, ω_j, γ_j and I_j are the peak position, halfwidth and area of the jth Raman band, respectively, N is the number of bands, and y_0 is the background level. Some of the Raman bands assigned to the Si two-phonon overtone states[51] are better modeled by asymmetric Lorentz function $LA(\omega)$ composed of the simple

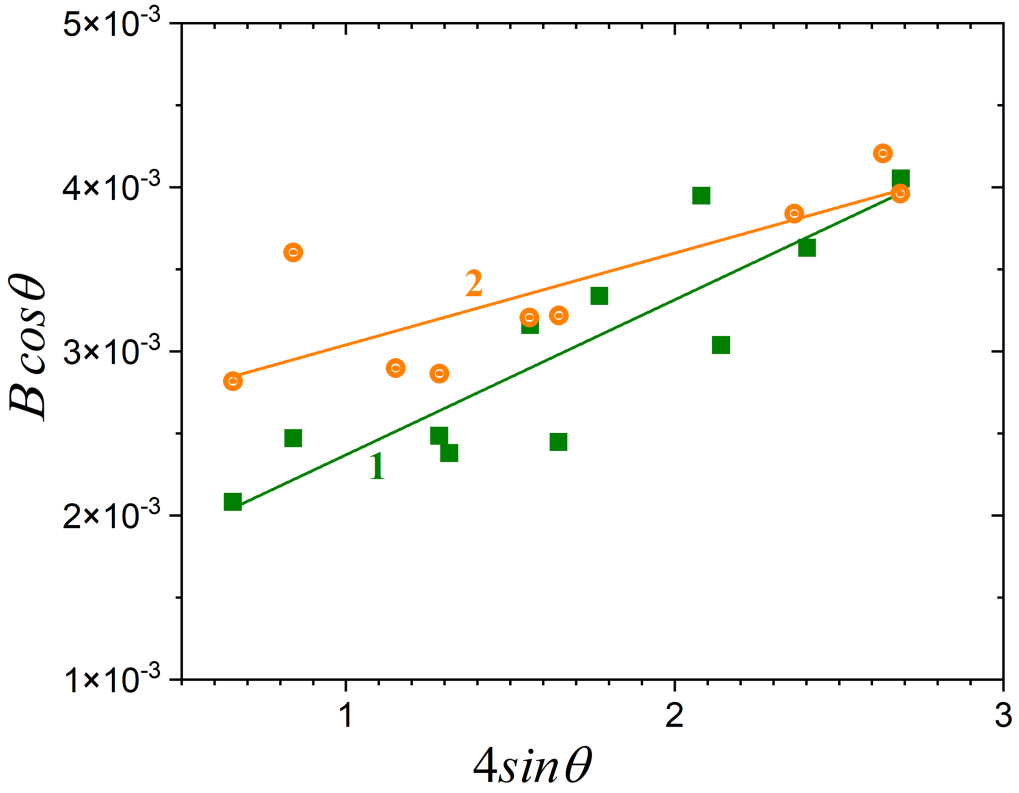

Figure 6. The Williamson-Hall analysis of the S1 (solid squares) and S2 (dotted circles) structures. Fit to the data, the strain is extracted from the slope and the crystalline size is extracted from the y-intercept of the fit. Linear fit is given by the following expressions: $y = 0.00094x + 0.00142$ for the S1 structure (1) and $y = 0.00056x + 0.00248$ for the S2 structure (2).

Table III. Comparison of the positions (cm^{-1}) and areas of β-Ga_2O_3 Raman bands.

	Film, ω_j		Single crystal, ω_{ref_j}				$\omega_j - \overline{\omega}_{ref_j}$		
Phonon mode	S1	S2	Ref. 56	Ref. 57	Ref. 58	$\overline{\omega}_{ref_j}$	S1	S2	$\frac{I_j(S2)}{I_j(S1)}$
$A_g^{(1)}$	110.3	110.8	111.4	110.7	111.0	111.0	−0.7	−0.3	0.8
$B_g^{(1)}$	114.2	114.5	114.8	114.3	114.8	114.6	−0.5	−0.2	0.7
$B_g^{(2)}$	144.6	145.0	145.5	144.9	144.8	145.1	−0.5	−0.1	1.0
$A_g^{(2)}$	169.6	169.9	170.4	169.8	169.9	170.0	−0.4	−0.2	1.0
$A_g^{(3)}$	200.3	200.4	200.9	200.3	200.2	200.5	−0.2	0.0	1.0
$A_g^{(4)}$	319.8	320.3	320.9	320.3	320.0	320.4	−0.6	−0.1	1.5
$A_g^{(5)}$	346.6	347.0	347.2	347.0	346.6	346.9	−0.4	0.1	0.5
$B_g^{(3)}$	354.7	353.4	353.5	353.4	353.2	353.4	1.3	0.1	2.0
$A_g^{(6)}$	416.6	416.5	417.0	416.7	416.2	416.6	−0.1	−0.1	1.3
$A_g^{(7)}$	475.4	475.3	475.6	475.3	474.9	475.3	0.1	0.0	0.7
$B_g^{(4)}$	476.8	479.0	476.6	475.9	474.9	475.8	1.0	3.2	6.4
$A_g^{(8)}$	629.5	630.8	630.4	630.4	630.0	630.3	−0.7	0.5	0.9
$B_g^{(5)}$	652.3	653.9	652.6	652.4	652.3	652.4	−0.1	1.5	1.5
$A_g^{(9)}$	658.0	660.5	658.5	659.0	658.3	658.6	−0.6	1.9	1.0
$A_g^{(10)}$	767.6	768.1	766.9	767.3	766.7	767.0	0.6	1.1	1.0

Lorentzian $L(\omega) = (1 + 4(\omega - \omega_j)^2/\gamma_j^2)^{-1}$ in such a way[55]

$$LA(\omega) = [L(\omega)]^{\nu} \text{for} \omega \leqslant \omega_j \text{ and } LA(\omega) = [L(\omega)]^{\xi} \text{ for } \omega > \omega_j, \quad [5]$$

where ν and ξ were different exponents raising the corresponding side of the Lorentzian.

Spectral β-Ga_2O_3 peak positions in the measured (ω_j) and reference (ω_{ref_j}) Raman spectra together with a shift from the averaged Refs. 56–58 value ($\overline{\omega}_{ref_j}$) and ratio of normalized areas

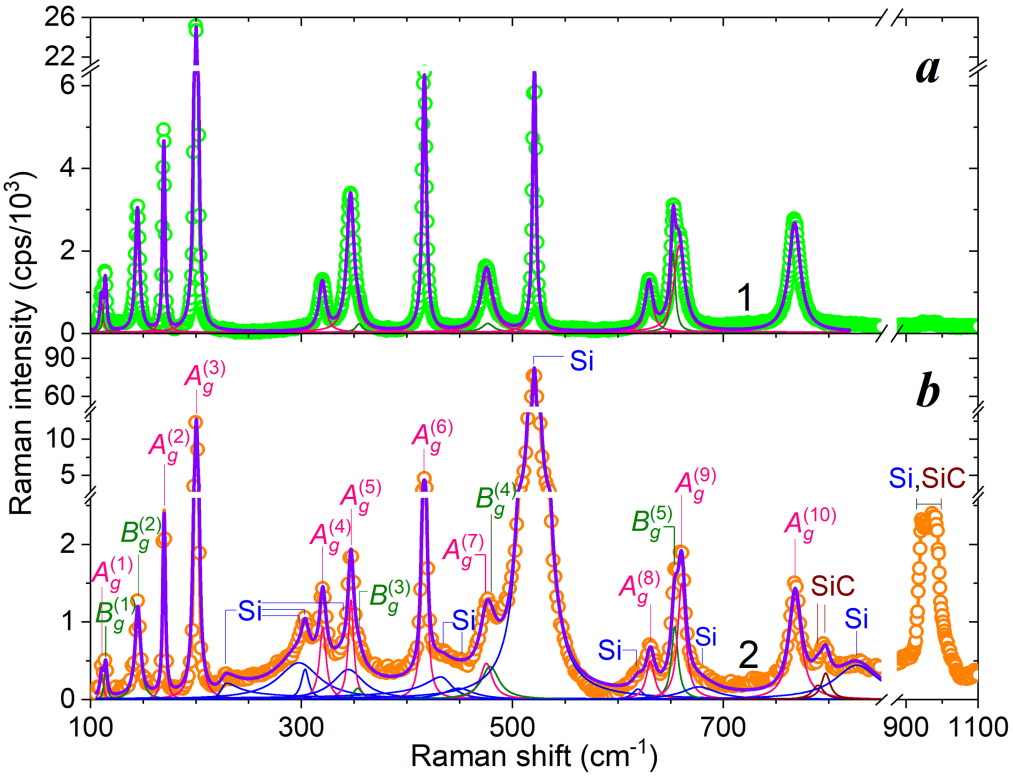

Figure 7. Raman spectra and their fitting results for the S1 (*a*) and S2 (*b*) structures. Measured curves are green (1) and orange (2), total calculated profile is violet, the other colored curves represent the β-Ga_2O_3 A_g and B_g modes as well as Si and SiC ones as indicated above them in the *b* part.

for the *j*th band in the S1 and S2 spectra given in Table III. The last right column shows the ratio of normalized areas (integrated intensities) for the *j*th Raman band in the S1 and S2 spectra. By normalization, in this case, we mean dividing the band area of the *j*th A_g or B_g phonon mode by the band area of the $A_g^{(3)}$ or $B_g^{(2)}$ mode, most strong in the corresponding representation. As can be seen from Table III, the frequencies of the β-Ga_2O_3 phonon modes in the spectra of both films remain practically unchanged relative to the average reference values $\overline{\omega}_{ref_j}$. The exception to this is a slight, no more than 2 cm^{-1}, shift for the high-frequency $B_g^{(5)}$, $A_g^{(9)}$ and $A_g^{(10)}$ modes that are assigned to the antisymmetric and symmetric stretching as well as bending vibrations of different GaO_2 groups in GaO_4 tetrahedrons.[50] Such behavior of these modes may be caused by some changes of lattice parameters discussed above (Table I). As for the 3.2 cm^{-1} $B_g^{(4)}$ mode shift, this could be attributed to the ambiguity of the fitting procedure due to its low intensity and the strong overlapping of the neighboring 475 cm^{-1} (β-Ga_2O_3) and 521 cm^{-1} (Si) modes with a much greater intensity (bottom part of Fig. 7). In any case, these shifts are much smaller than those, ranging from 10 cm^{-1} to 40 cm^{-1}, observed for gallium oxide nanowires and caused by internal strains.[59] Being critical of the intensity variations for some B_g modes for the reasons just described, we can ascertain that the parameters of β-Ga_2O_3 optical modes remain largely unchanged when altering the film thickness together the Si wafer orientation.

Conclusions

In this paper we have demonstrated the possibility of growing the 1.15 μm and 2.25 μm β-Ga_2O_3 films on SiC/porous Si/Si substrates using high-frequency magnetron sputtering technique. The deposited β-Ga_2O_3 films are found to have a polycrystalline structure with an average crystallite size of 62 nm and 109 nm. Most of the crystallites are preferentially oriented along the [100] direction as the other preferred orientations along [401], [101] and [201] directions might be also considered. The relative changes in β-Ga_2O_3 crystallite lattice parameters do not exceed 1.5×10^{-3}, with a more deviation for thicker film, and the estimated strain ε values are no higher than 1×10^{-3}. The fitting of the Raman spectra reveals no significant discrepancies between the parameters of phonon modes both in our β-Ga_2O_3 films and the corresponding single crystal. Thus, the further application of the magnetron sputtering technique for growing β-Ga_2O_3 films with thicknesses ranging from tens of nanometers to tens of micrometers appears to be feasible. In this case, as follows from the results obtained, it is possible to deposit the films on non-native substrates, in particular, silicon substrates, without the appearance of significant internal stresses and considerable changes in lattice parameters, which is especially important to meet the modern needs of micro- and optoelectronics.

The successful fabrication of β-Ga_2O_3 thin films on Si substrates demonstrates the potential for integrating ultra-wide bandgap materials with silicon-based platforms. To advance the practical use of such heterostructures, further studies will focus on electrical characterization of Schottky and MOS structures, analysis of interface states, and stability under high electric fields and thermal cycling. Investigation of charge transport mechanisms and optical response under UV illumination will also be carried out to evaluate device-level applicability. The use of β-Ga_2O_3 in power electronics can increase the energy efficiency of devices, reducing indirect impacts on climate and resources. Although gallium oxide is not currently subject to strict environmental regulation, its production and utilization should be controlled, especially in the nanoform. Further research on its environmental safety and bioaccumulation is needed.

Acknowledgments

The research was supported by the German Research Foundation under the Walter Benjamin Programme, referenced as KI 2865/1-1. A. S. Revenko acknowledges funding from Science Foundation Ireland under the Supplemental Grant for Displaced Researchers scheme (SFI 20/FFP-P/8728 (S)).

ORCID

M. P. Derhachov https://orcid.org/0000-0002-8627-6678
A. S. Revenko https://orcid.org/0009-0009-4147-1179
O. I. Gudymenko https://orcid.org/0000-0002-5866-8084

References

1. H. H. Radamson et al., *Micromachines*, **10**, 293 (2019).
2. R. K. Ratnesh, A. Goel, G. Kaushik, H. Garg, Chandan, M. Singh, and B. Prasad, *Mater. Sci. Semicond. Process.*, **134**, 106002 (2021).
3. B. Morkoc, A. Kahraman, and E. Yilmaz, *Mater. Chem. Phys.*, **292**, 126875 (2022).
4. K. Oishi, D. Akai, and M. Ishida, *Solid. State. Electron.*, **103**, 110 (2015).
5. Y. H. Lee, H. Song, K.-H. Kim, and J. Oh, *APL Mater.*, **7**, 071106 (2019).
6. Y. Kang, H. Deng, Y. Chen, Y. Huo, J. Jia, L. Zhao, Z. Zaidi, K. Zang, and J. S. Harris, *IEEE Photonics J.*, **11**, 1 (2019).
7. S. Li, Y. Zhang, D. Yang, W. Yang, X. Chen, H. Zhao, J. Hou, and P. Yang, *Phys. B Condens. Matter*, **584**, 412065 (2020).
8. Y. H. Wong and K. Y. Cheong, *J. Mater. Sci., Mater. Electron.*, **21**, 980 (2010).
9. X.-R. Wang, Y.-X. Zeng, J. Zhang, W. Huang, H.-P. Ma, and Q.-C. Zhang, *Mater. Res. Express*, **11**, 015902 (2024).
10. J. Åhman, G. Svensson, and J. Albertsson, *Acta Crystallogr. Sect. C*, **52**, 1336 (1996).
11. L. Aarik, H. Mändar, A. Kasikov, A. Tarre, and J. Aarik, *J. Mater. Chem. C*, **12**, 10562 (2024).
12. M. Baldini, Z. Galazka, and G. Wagner, *Mater. Sci. Semicond. Process.*, **78**, 132 (2018).
13. C. Zhang, X. Fu, and H. Wang, *Mater. Today Commun.*, **40**, 109994 (2024).
14. M. J. Tadjer, J. L. Lyons, N. Nepal, J. A. Freitas, A. D. Koehler, and G. M. Foster, *ECS J. Solid State Sci. Technol.*, **8**, Q3187 (2019).
15. Z. Guo and Y. Mao, *Vacuum*, **234**, 114057 (2025).
16. Y. Wu, X. Yan, Y. Jiang, T. Yao, C. Chen, and H. Ye, *Thin Solid Films*, **796**, 140336 (2024).
17. F. Amraoui and N. Sengouga, *J. Sol-Gel Sci. Technol.*, **111**, 1 (2024).
18. T. Li, G. Liu, H. Kong, G. Yang, G. Wei, and X. Zhou, *Coord. Chem. Rev.*, **475**, 214909 (2023).
19. K. Saikumar, S. D. Nehate, and K. B. Sundaram, *ECS J. Solid State Sci. Technol.*, **8**, Q3064 (2019).
20. D. Guo, Q. Guo, Z. Chen, Z. Wu, P. Li, and W. Tang, *Mater. Today Phys.*, **11**, 100157 (2019).
21. F. Shi and H. Qiao, *Nano Sel.*, **3**, 348 (2022).
22. H. Chen et al., *Semicond. Sci. Technol.*, **39**, 063001 (2024).
23. X. Chen, F.-F. Ren, J. Ye, and S. Gu, *Semicond. Sci. Technol.*, **35**, 023001 (2020).
24. H. Zhang, L. Yuan, X. Tang, J. Hu, J. Sun, Y. Zhang, Y. Zhang, and R. Jia, *IEEE Trans. Power Electron.*, **35**, 5157 (2020).
25. C. Venkata Prasad and Y. S. Rim, *Mater. Today Phys.*, **27**, 100777 (2022).
26. N. S. Jamwal and A. Kiani, *Nanomaterials*, **12**, 2061 (2022).
27. J. Liang, D. Takatsuki, M. Higashiwaki, Y. Shimizu, Y. Ohno, Y. Nagai, and N. Shigekawa, *Jpn. J. Appl. Phys.*, **61**, SF1001 (2022).
28. R. Wu, K. Zhou, C. Y. Yue, J. Wei, and Y. Pan, *Prog. Mater Sci.*, **72**, 1 (2015).
29. H. Wang et al., *Mater. Sci. Semicond. Process.*, **178**, 108422 (2024).
30. L. M. Soltys, I. F. Mironyuk, I. M. Mykytyn, I. D. Hnylytsia, and L. V. Turovska, *Phys. Chem. Solid State*, **24**, 5 (2023).
31. N. Naderi and M. Moghaddam, *Ceram. Int.*, **46**, 13821 (2020).
32. M. Kamiński et al., *Materials (Basel)*, **18**, 12 (2025).
33. H. Okumura, M. Kita, K. Sasaki, A. Kuramata, M. Higashiwaki, and J. S. Speck, *Appl. Phys. Express*, **7**, 095501 (2014).
34. Z. Zhang, P. Yan, Q. Song, H. Chen, W. Zhang, H. Yuan, F. Du, D. Liu, D. Chen, and Y. Zhang, *Fundam. Res.*, **4**, 1292 (2024).
35. T. Kusaba, P. Sittimart, Y. Katamune, T. Kageura, H. Naragino, S. Ohmagari, S. M. Valappil, S. Nagano, A. Zkria, and T. Yoshitake, *Appl. Phys. Express*, **16**, 105503 (2023).
36. V. V. Kidalov, A. F. Dyadenchuk, V. P. Kladko, O. I. Gudymenko, M. P. Derhachov, S. O. Popov, O. O. Sushko, and V. V. Kidalov, *ECS J. Solid State Sci. Technol.*, **11**, 025004 (2022).
37. V. Lehmann, R. Stengl, and A. Luigart, *Mater. Sci. Eng.*, **B 69–70**, 11 (2000).
38. H. Föll, M. Christophersen, J. Carstensen, and G. Hasse, *Mater. Sci. Eng. R Reports*, **39**, 93 (2002).
39. V. V. Kidalov, S. A. Kukushkin, A. V. Osipov, A. V. Redkov, A. S. Grashchenko, I. P. Soshnikov, M. E. Boiko, M. D. Sharkov, and A. F. Dyadenchuk, *ECS J. Solid State Sci. Technol.*, **7**, 158 (2018).
40. V. V. Kidalov, A. S. Revenko, D. Duleba, R. A. Redko, M. Assmann, A. I. Gudimenko, and R. P. Johnson, *ECS J. Solid State Sci. Technol.*, **13**, 114003 (2024).
41. V. V. Kidalov, A. F. Dyadenchuk, V. A. Baturin, O. Y. Karpenko, O. F. Kolomys, V. V. Ponomarenko, Z. V. Maksimenko, V. V. Strelchuk, Y. Y. Bacherikov, and O. B. Okhrimenko, *Semicond. Physics, Quantum Electron. Optoelectron.*, **26**, 140 (2023).
42. V. Kidalov, A. Dyadenchuk, C. Abbasova, V. Baturin, O. Karpenko, O. Gudimenko, and V. Kidalov, *IEEE 12th Int. Conf. Nanomater. Appl. Prop.*1 (2022), 10.1109/NAP55339.2022.9934602.
43. S. A. Kukushkin, K. K. Nussupov, A. V. Osipov, N. B. Beisenkhanov, and D. I. Bakranova, *Phys. Solid State*, **59**, 1014 (2017).
44. S. A. Kukushkin, K. K. Nussupov, A. V. Osipov, N. B. Beisenkhanov, and D. I. Bakranova, *Superlattices Microstruct.*, **111**, 899 (2017).
45. W. A. Dollase, *J. Appl. Crystallogr.*, **19**, 267 (1986).
46. E. Zolotoyabko, *J. Appl. Crystallogr.*, **42**, 513 (2009).
47. J. Rodríguez-Carvajal, *IUCr Comm. Powder Diffr. Newsl.*, **26**, 12 (2001).
48. S. Husain and A. O. A. Keelani, *Mater. Today Proc.*, **5**, 5615 (2018).
49. J. Madhavi, *SN Appl. Sci.*, **1**, 1509 (2019).
50. D. Dohy, G. Lucazeau, and A. Revcolevschi, *J. Solid State Chem.*, **45**, 180 (1982).
51. K. Uchinokura, T. Sekine, and E. Matsuura, *J. Phys. Chem. Solids*, **35**, 171 (1974).
52. S. Sanna, J. Plaickner, K. Holtgrewe, V. M. Wettig, E. Speiser, S. Chandola, and N. Esser, *Materials*, **14**, 4104 (2021).
53. H. Harima, *Microelectron. Eng.*, **83**, 126 (2006).
54. M. Derhachov, V. Moiseienko, N. Kutseva, B. Abu Sal, and R. Holze, *Eur. Phys. J. Plus*, **134**, 370 (2019).
55. G. H. Major et al., *Surf. Interface Anal.*, **53**, 689 (2021).
56. B. M. Janzen, R. Gillen, Z. Galazka, J. Maultzsch, and M. R. Wagner, *Phys. Rev. Mater.*, **6**, 54601 (2022).
57. B. M. Janzen, P. Mazzolini, R. Gillen, A. Falkenstein, M. Martin, H. Tornatzky, J. Maultzsch, O. Bierwagen, and M. R. Wagner, *J. Mater. Chem. C*, **9**, 2311 (2021).
58. C. Kranert, C. Sturm, R. Schmidt-Grund, and M. Grundmann, *Sci Rep.*, **6**, 35964 (2016).
59. R. Rao, A. M. Rao, B. Xu, J. Dong, S. Sharma, and M. K. Sunkara, *J. Appl. Phys.*, **98**, 094312 (2005).